FULL SCALE ROTOR AEROACOUSTIC PREDICTIONS AND THE LINK TO MODEL SCALE ROTOR DATA

D. Douglas Boyd, Jr.
Aerospace Engineer
Aeroacoustics Branch
AAAC
David.D.Boyd@nasa.gov

Casey L. Burley
Aerospace Engineer
Aeroacoustics Branch
AAAC
Casey.L.Burley@nasa.gov

David A. Conner
Aerospace Engineer
Aeroflightdynamics Directorate (AMRDEC)
RD&E Command / U.S. Army
David.A.Conner@nasa.gov

NASA Langley Research Center
Hampton, VA 23681

Abstract

The NASA Aeroacoustic Prediction System (NAPS) is used to establish a link between model-scale and full-scale rotor predictions and is partially validated against measured wind tunnel and flight aeroacoustic data. The prediction approach of NAPS couples a comprehensive rotorcraft analysis with acoustic source noise and propagation codes. The comprehensive analysis selected for this study is CAMRAD-II, which provides the performance/trim/wake solution for a given rotor or flight condition. The post-trim capabilities of CAMRAD-II are used to compute high-resolution sectional airloads for the acoustic tone noise analysis, WOPMOD. The tone noise is propagated to observers on the ground with the propagation code, RNM (Rotor Noise Model). Aeroacoustic predictions are made with NAPS for an isolated rotor and compared to results of the second Harmonic Aeroacoustic Rotor Test (HART-II) program, which tested a 40% dynamically and Mach-scaled BO-105 main rotor at the DNW. The NAPS is validated with comparisons for three rotor conditions: a baseline condition and two Higher Harmonic Control (HHC) conditions. To establish a link between model and full-scale rotor predictions, a full-scale BO-105 main rotor input deck for NAPS is created from the 40% scale rotor input deck. The full-scale isolated rotor predictions are then compared to the model predictions. The comparisons include aerodynamic loading, acoustic levels, and acoustic pressure time histories for each of the three conditions. With this link established, full-scale predictions are made for a range of descent flight conditions and compared with measured trends from the recent Rotorcraft Operational Noise Abatement Procedures (RONAP) flight test conducted by DLR and ONERA. Additionally, the effectiveness of two HHC conditions from the HART-II program is demonstrated for the full-scale rotor in flight.

Notation

BPF	Blade passage frequency
BVI	Blade-vortex interaction
C_N	Normal force coefficient
dB	Decibel level
dBA	A-weighted decibel level
L_A	Overall sound pressure level [dBA]
M	Mach number
mid-SPL	SPL from 6th to 40th BPF
OASPL [dBA]	Overall Sound Pressure Level
HHC	Higher harmonic control
M	Mach number
R_{FS}	Full-scale rotor radius = 5.0 [m]
R	Model-scale rotor radius = 2.0 [m]
SPL	Sound pressure level [dB]
T1C	Cosine component of cyclic pitch
T1S	Sine component of cyclic pitch
T75	Collective pitch at 0.75R
T_{REV}	Rotor period [sec]
x, y	Linear distance [m]

Presented at the AHS 4th Decennial Specialists' Conference on Aeromechanics, San Francisco, CA, Jan. 21-23, 2004.

Introduction

Rotary wing vehicles have been identified as a class of vehicles with the potential to increase the capacity of the air transportation system. For rotary wing vehicles to become a viable part of the transportation system, they must be perceived by the public as a quiet, safe, economical mode of transportation. Though there are many barriers associated with introducing a new class of vehicles

into the transportation system, noise has been identified as a major barrier for the introduction of rotary wing vehicles (Ref. 1).

In an effort to understand and ultimately control rotorcraft noise, many experimental and computational studies have been performed over the last several decades to characterize the noise from rotorcraft and to explore noise reduction concepts (Ref. 2). Experimental studies have included both wind tunnel tests (model-scale and full-scale) and flight tests. Typically, wind tunnel tests have been used to improve basic understanding of noise sources and to quantify the effectiveness of noise reduction concepts (Refs. 3, 4, 5), while flight tests have been used to examine the community noise implications of various operational procedures (Refs. 6, 7, 8, 9). Experimentally, researchers have carefully linked model scale measured acoustic data to full-scale measured acoustic data (Refs. 2, 10) for several noise mechanisms. For the blade-vortex interaction (BVI) mechanism, Schmitz, *et al* (Ref. 10) established that there are four key scaling parameters that must be matched when comparing model and full-scale data. These parameters are the rotor advance ratio, hover tip Mach number, thrust coefficient, and rotor tip-path plane angle.

Prediction efforts normally have followed the same path as experimental efforts. That is, wind tunnel predictions typically are used to aid in the basic understanding of noise sources (Ref. 11) and flight predictions (Ref. 12) are used to assess vehicles undergoing operational variations. Though wind tunnel noise predictions for isolated rotors are now starting to provide an excellent engineering level of accuracy (Refs. 11, 13), flight predictions are still in their infancy (Refs. 12, 14, 15) and many challenges still remain (Ref. 16). Though References 2 and 10 established links between model and full-scale measured data, the same type of link for noise prediction has not been fully established to-date for BVI noise. The purpose of this paper is to establish this prediction link.

The need for this prediction link is that, despite the challenges discussed in Reference 16, there remains a need to predict and assess the community noise impact of rotary wing flight vehicles and/or noise reduction concepts. To begin to address this need, an assessment of the current ability to predict noise from a rotor in flight must be made. To make this assessment, while minimizing the difficulties introduced in Reference 16, predictions are compared to scale model results from the second Harmonic Aeroacoustics Rotor Test (HART-II) program and to full-scale results from the Rotorcraft Operational Noise Abatement Procedures (RONAP) flight test. HART-II is a cooperative wind tunnel rotor test effort involving DLR of Germany, ONERA of France, and both AFDD and NASA of the United States (Refs. 17, 18). The HART-II effort has resulted in benchmark measurements of the rotor acoustics, blade loads and motion, and wake geometry and strength for a 40% dynamically and Mach-scaled BO-105 main rotor. The RONAP flight test was conducted by DLR and ONERA as part of the ONERA-DLR Partnership Agreements on Rotorcraft Research (Ref. 9). In the RONAP flight test, a BO-105 rotorcraft equipped with a highly instrumented main rotor was flown for a number of different flight conditions to provide data for noise abatement procedure studies, for prediction code validation, and for comparison with wind tunnel data. Specific conditions were flown to closely match a baseline condition from the HART-II wind tunnel program. Speigel, *et al* (Ref. 9) recently presented the measured flight data. A subset of the measured results is used here to assess the predicted results.

This paper takes the following steps. First, measured rotor loading and acoustic data from the HART-II wind tunnel test of an isolated BO-105 model rotor in a "maximum blade-vortex interaction (BVI) noise" descent condition are used to demonstrate the capabilities of the NASA Aeroacoustic Prediction System (NAPS). With the level of fidelity demonstrated for a model scale rotor in a wind tunnel, the entire prediction method is scaled-up to match a full-scale representation of the same isolated rotor. Scaling of the prediction method in this manner allows a direct link that facilitates comparison of the full-scale predicted data to the model scale predicted and measured data. Using this link, the same model-scale prediction fidelity is then demonstrated for the full-scale isolated rotor. With the connection established between the model scale rotor and the full-scale rotor, predicted acoustic trends with descent angle variations are compared to available measured acoustic trends from the RONAP flight test. Finally, full-scale rotor predictions are carried out with higher harmonic control (HHC) conditions from the HART-II wind tunnel test to demonstrate the effectiveness of HHC when used in full-scale flight conditions.

Current Prediction Method

In general, rotorcraft acoustic prediction methods (Ref. 16) include a rotorcraft aeromechanics model which computes the rotorcraft trim (including rotorcraft and blade airloads and motion), a high-resolution reconstruction method which computes airloads and motion at a resolution adequate for an acoustic prediction, and an acoustic model which computes the noise at specified observer locations (see Figure 1). The NAPS includes all of the above components and is described briefly here.

Aeromechanics and Reconstruction Model

For the rotorcraft aeromechanics model, NAPS uses CAMRAD-II (Ref. 19). CAMRAD-II is a comprehensive rotorcraft aeromechanics model that couples aerodynamics, dynamics, and flight dynamics and computes the "trim" state of the vehicle, given a flight condition. A finite element beam model is used to compute the fully coupled flap, lag, pitch, and axial (extension) motion of rotor blades. Blade aerodynamics are accounted for using a second-order lifting line model, including effects of compressibility, yawed flow, blade sweep, Reynolds number, reverse flow, and dynamic stall. The rotor vortex wake is computed using a full-span free vortex-wake model. The free wake method uses multiple trailed vortex elements along the blade span (17 trailed vortices are used in this study). Roll-up of the distant vortex wake elements is modeled using a vortex "consolidation" model (Ref. 20). In addition, each of these models can account for multiple rotors, and airframe aerodynamics and dynamics.

The aerodynamic and dynamic quantities discussed above are computed at a resolution appropriate for determining vehicle trim state. Typically, the trim state is computed with 15° time step (azimuthally). However, the resolution for airloads and blade motion that is required for acoustic computations is substantially higher than that required for determination of the trim state. For efficiency, CAMRAD-II employs a "post-trim" computation at the end of the trim stage to determine the high-resolution blade motion and airloads required for the subsequent acoustic computations. The post-trim procedure uses the blade motion from the last trim iteration to determine all high-resolution blade motion information. Because the blade motion is known as a function of harmonics, the post-trim procedure computes the blade position at any azimuthal time step, as needed, by evaluating harmonics. The wake geometry is comprised of an undistorted helical wake to which a distorted free wake is added. The distorted component of the wake geometry in the post-trim procedure typically is computed at the same resolution as the trim computation, using the circulation and blade motion information from the previous trim stage. The undistorted helical wake is first computed at the high resolution. Then, the distorted components of the wake are linearly interpolated in time and wake age (that is, element-by-element) before being added onto the undistorted helical wake at the appropriate time and wake age. All other information, such as circulation, is linearly interpolated in a consistent manner. The high-resolution influence coefficients and rotor loading are finally computed as the rotor is stepped through the higher resolution azimuth increments.

Acoustics Model (Tone Noise)

There are a number of noise sources associated with rotorcraft. For example, in certain descent conditions, BVI noise is dominant. In fast forward flight cases, high-speed impulsive (HSI) noise due to shocks can be dominant. In some climb conditions, broadband noise sources (*e.g.*, blade-wake interactions (BWI) noise) can be significant. Other noise sources, such as engine noise, tail rotor noise, and airframe noise can exist as well. In this paper, since we are considering descent conditions for which the BVI noise is known to be dominant, we will only examine tone noise.

For the current method, rotor tone noise is predicted using WOPMOD, which is a modified version of the WOPWOP (Ref. 21) computer code. Given high-resolution rotor blade airloads, motion, and geometry, WOPMOD computes thickness and loading tone noise in the form of acoustic pressure time histories at given observer locations. For wind tunnel computations, these observer locations correspond to the microphone measurement locations, which are in close enough proximity of rotor such that atmospheric propagation effects are negligible.

For flight computations, it is necessary to include atmospheric propagation effects at relatively large distances from the noise source. To accomplish this, the noise computations for a flight vehicle are preformed in two steps. First, the tone noise is computed on a hemispherical surface below the vehicle. For this paper, the hemispherical surface is placed at a radius of $10R_{FS}$ from the rotor center. This is close enough to the vehicle that atmospheric effects are still negligible. Second, accounting for atmospheric effects, the data on the noise hemisphere are propagated to distant observers locations.

Atmospheric Propagation

The Rotorcraft Noise Model (Refs. 22, 23) is used to account for atmospheric propagation effects. The analytical techniques are similar to those used in the NASA Aircraft Noise Prediction Program (ANOPP) (Ref. 24). In RNM, acoustic data on noise hemispheres are propagated to ground based observer locations while accounting for geometrical spherical spreading losses, atmospheric absorption losses, ground reflection and attenuation effects, terrain effects, Doppler shifting, phase differences between direct and reflected rays, and vehicle attitude and flight track variations. Currently, RNM assumes that the acoustic ray paths are straight lines and that no wind is present. Atmospheric absorption losses are accounted for using the ANSI/ISO standard (Ref. 25). Corrections for ground reflection and attenuation losses, caused by the ground and the resultant interaction between direct and reflected acoustic rays,

are based on a study made by Chien and Soroka (Ref. 26) and Chessel (Ref. 27) with corrections noted by Daigle (Ref. 28). The ground surface is characterized as a complex acoustic impedance and the algorithm uses the Doppler-shifted frequencies that are based on the speed and direction of the aircraft relative to the receiver. Corrections for topographic effects caused by the reflection and absorption that occurs from barriers formed by the terrain located between the source and the receiver use an implementation of the geometrical theory of diffraction as developed by Rasmussen (Ref. 29). This method can account for hills, valleys, vertical barriers, and non-uniform ground impedance (*e.g.*, water or land). However, echo effects (*e.g.*, from deep canyons, or from surfaces behind the receiver relative to the source) are not presently treated by RNM.

RNM computes a noise metric time history at a single observer position, the noise footprint on the ground at a given instance in time, and noise contours for many different noise metrics. RNM can also generate results suitable for importation into a Geographical Information System (GIS) for land-use planning studies. RNM has been validated in the audible frequency range using data acquired during a number of different flight test programs.

Experiment

Measured data from the Higher Harmonic Control Aeroacoustics Rotor Test (HART-II) (Ref. 17, 18) is used to demonstrate the fidelity of the method described above. Lim, *et al* (Ref. 13) recently presented the measured data used herein. The HART-II test quantified the acoustic footprint near a four-bladed, rectangular planform, isolated, 40% dynamically scaled model of a BO-105 rotor in a descent condition. The test examined this rotor with and without HHC of blade pitch. Measurements of blade aerodynamic loading were made at several blade sections. The rotor operating condition was held at a constant flight condition equivalent to a 6° descent, which is a descent condition where BVI noise dominates. The rotor was trimmed to a nominal thrust coefficient of 0.0044, while the hub roll and pitch moments were nominally trimmed to zero. To demonstrate the fidelity of the prediction scheme, three different conditions are examined from this test. These three conditions are (1) a baseline (BL) condition without HHC, (2) a minimum noise (MN) condition, and (3) a minimum vibration (MV) condition. The BL case did not use HHC. Both the MN and MV cases employed a HHC pitch with 3 pitch cycles per rotor revolution that was superimposed on the primary rotor pitch control. For both cases, the nominal HHC amplitude was 0.8°. The cases differ in the phasing of the HHC pitch cycles with respect to the rotor azimuth. For the MN and MV cases, the first minimum in the HHC pitch is located at azimuth angles of 40° and 0°, respectively. In the MN case, HHC was used to lower the mid-frequency sound pressure level (mid-SPL) noise on the advancing side of the rotor in the microphone plane below the rotor system. In the MV case, HHC was used to minimize the four per-revolution vertical component of vibration at the rotor hub. Predicted results for these three cases will be presented next.

Results: Model scale

Aerodynamics:

During HART-II (Ref. 17, 18), blade pressures were measured at several radial stations on the blade. A full chord-wise set of pressure taps was located at 0.87R. These quantities have been integrated and are displayed in Figure 2 as a normal force coefficient multiplied by the local Mach number squared, $C_N M^2$. The figure shows measured and predicted normal force times the local Mach number squared at 0.87R, as a function of rotor blade azimuth location, for the BL case. It can be seen from this plot that the primary features of the measured data are captured in the prediction. Multiple predicted BVI events, similar to the measured data, can be seen in the first and fourth quadrants.

Figure 3 shows the normal force coefficient times local Mach number squared for the MN condition. In both the measured and predicted data, the low frequency loading has been increased substantially; the BVI events are still seen, but they are reduced in magnitude; this trend is captured well in the predicted data. Figure 4 compares measured and predicted loading in the same manner as the previous two figures. Here, the BVI events are captured, though the low frequency loading component is not as well captured as in the MN prediction.

Mid-SPL:

Model scale predicted noise contours are computed and compared to the measured model data. Figure 5 shows the measured and predicted mid-SPL footprint, 2.15R below the rotor, for the BL condition. (The mid-SPL is defined here as the sound pressure level computed using only the 6th through the 40th harmonics of the blade passage frequency.) The vertical axis represents the microphone traverse stream-wise position divided by the rotor radius, R. Negative numbers on this axis are up-stream of the rotor; positive numbers are downstream. The horizontal axis represents the lateral microphone position divided by rotor radius. Negative numbers are on the retreating side of the rotor; positive numbers are on the advancing side. For reference purposes, the black circle in each plot depicts the

rotor radius and the small black square on the advancing side of the rotor marks the location where acoustic pressure time histories will be examined later. The measured data shows the typical elevated mid-frequency noise levels below the second and fourth rotor quadrants due to BVI. The predicted results show the same elevated level trends. The noise directivity pattern is well represented by the prediction; however, the amplitude of the predicted noise is approximately 2 to 3 dB higher than the measured noise. This is consistent with the over-prediction of the peak-to-peak variation of BVI events in the previous BL C_NM^2 plot. The rapid decrease in measured noise levels on the upstream, retreating side of the rotor (3rd quadrant) is attributable to noise shielding from the fuselage; this effect is not accounted for in the predictions.

Figure 6 shows the measured and predicted mid-SPL for the MN condition. The measured HHC for this condition was set to reduce the noise on the advancing side of the rotor as much as possible for this particular type, frequency, and amplitude of HHC. In the prediction, the trim state was computed with the measured HHC superimposed on the blade pitch control variable. Relative to the measured BL case, the measured MN case reduces the peak mid-SPL on the advancing side by approximately 2 dB while shifting the location, or directivity, of the peak noise toward the forward portion of the rotor. The predicted noise for this case also has a peak mid-SPL on the advancing side that is several dB lower than the predicted BL noise in the same region. Though the dB levels are still slightly higher than the measured data, the noise reduction trends of the measured data are captured in the prediction.

Figure 7 shows the measured and predicted mid-SPL for the MV case. The measured HHC was set such that the four-per-revolution vertical vibration component at the rotor hub was minimized for this particular type, frequency, and amplitude of HHC. Again, this measured HHC was superimposed on the blade pitch control variable used to compute the trim state; therefore, it is included in the trim state computation. As with the BL and MN cases, the measured and predicted acoustic trends well match the increase in mid-SPL on the advancing side for this case.

In general, relative decibel changes between the predicted BL case and the MV and MN cases are consistent with the changes seen in the measured rotor model data, though absolute noise levels are slightly different. The directivity pattern changes between the predicted cases are not as well matched to the measured changes, particularly for the MN case.

Acoustic pressure time histories:

In addition to the integrated noise levels seen above, it is important to examine the acoustic pressure time histories to provide evidence that the correct physical phenomena are being captured by the predictions (Ref. 16). Figure 8 shows the acoustic pressure time history at the advancing-side location indicated in Figure 5. On the vertical axis is the acoustic pressure, displayed in Pascals. On the horizontal axis is the observer time divided by the rotor period (*i.e.*, the time required to complete one rotor revolution, T_{REV}). The measured data shows nearly identical (repeatable) BVI events for each of the four blades during the rotor revolution. The predicted data shows similar BVI events. However, between the BVI events, there is more low frequency content than in the measured data. There is additional mid-frequency content between the BVI pulses that contributes to the over-prediction of acoustic levels seen in the previous contour plots.

Figure 9 shows the acoustic pressure time history for the MN condition. This figure shows that the low frequency acoustic pressure caused by the HHC is well captured in magnitude and phase. The measured BVI events show more blade-to-blade differences than those in the BL case. Regardless, the predicted time history captures the primary physical features present in the measure data.

Figure 10 shows the acoustic pressure time history for the MV case. Even though the integrated mid-SPL noise contours match the measured data well (see Figure 7), the acoustic pressure time histories are not quite as well matched. The mid-frequency, multiple BVI content of the time history matches the measured data relatively well, but the low frequency content of the signal is not as well predicted as in the MN case. This trend is consistent with the under-prediction of the low frequency loading component seen in the C_NM^2 plot.

Results: Full-scale

The previous section demonstrated the ability of the current prediction scheme to predict model scale data. In this section a solid link will be made between model scale predictions and full-scale predictions. Dynamically scaling the entire prediction from a model-scale to a full-scale rotor, then comparing model-scale predictions to full-scale predictions, will facilitate this link.

Matching model scale

Though there are numerous ways to convert model scale predicted data into full-scale data, this paper takes advantage of the fact that the model rotor is a 40% dynamically scaled version of the full-scale rotor. In addition, from experimental data, Schmitz, *et al* (Ref. 10) presents a number of parameters that

must be matched for this type of comparison. These parameters are matched here for the predictions as well.

Using the fact that the model rotor is approximately a 40% dynamically scaled version of the full-scale rotor, the full-scale prediction is created from the model scale input information by appropriate scaling of the input parameters. The following scaling issues are performed. Geometrically, the radius and chord are scaled to full-scale, thereby matching the model rotor solidity. It should be noted that when the wind tunnel model rotor was developed, the model scale chord was increased by 10%, relative to the 40% scaling law, in order to better match the full-scale Reynolds number. For this study, that effect is not taken into account. This is because, for a study of this nature, it is more important to match rotor solidity because solidity is more directly related to overall rotor loading. Further, the difference in full-scale Reynolds number introduced by directly scaling from the model rotor chord to the full-scale rotor chord should have a negligible effect on the full-scale noise prediction used here. To match compressibility effects, the hover tip Mach number is matched with the model scale by decreasing the rotational speed of the full-scale rotor. The thrust coefficient divided by rotor solidity is matched to the model scale.

For blade dynamics, the Lock number is matched. To accomplish this, the mass distribution is scaled, while maintaining the same relative radial distribution. The remaining blade elastic properties are scaled using their respective definitions along with the 40% scaling, again while maintaining the same relative radial distribution as the model rotor for each parameter.

By scaling in this manner, it is expected that the predicted natural frequencies will be well matched between the model and full-scale rotors. Table 1 lists the predicted model and full-scale rotor natural frequencies of interest. Based on this matching and on the fact that the model rotor and input blade properties for the model rotor in CAMRAD-II were designed to match the first few natural frequencies of the full-scale rotor (Ref. 13), the full-scale predicted blade motions should be representative of a full scale rotor.

In addition to the scaling of the rotor input deck for the comprehensive analysis, the observer locations are scaled to maintain the same relative distance from the rotor as that used in the model scale predictions.

	Frequency [per-rev]	
Mode No.	Model	Full-scale
1	0.786	0.782
2	1.111	1.110
3	2.800	2.800
4	4.430	4.430
5	4.604	4.588
6	5.030	5.025
7	7.806	7.802
8	11.199	11.132

Table 1: Comparison of predicted model scale and full-scale rotor natural frequencies.

Trim differences:

Since the 40% scaling rule cannot be maintained for every parameter, some differences in the trim states for the model and full-scale rotors are expected. Another source of differences is introduced by the "trim tolerance". This trim tolerance is used by the comprehensive analysis to determine when the rotor is close enough to the target trim state such that no more iteration is necessary. To examine and quantify some of these differences, basic trim parameters (*e.g.*, rotor collective and cyclic pitch control settings) are compared.

	T75[°]	T1C[°]	T1S[°]
Measured			
BL	3.42	1.92	-1.34
MN	3.51	2.00	-1.35
MV	3.40	2.00	-1.51
Model			
BL	3.69	1.45	-1.27
MN	3.74	1.51	-1.17
MV	3.64	1.41	-1.28
Full			
BL	3.61	1.39	-1.44
MN	3.70	1.48	-1.18
MV	3.56	1.38	-1.38

Table 2: Comparison of measured and predicted rotor pitch control settings for the BL, MN, and MV conditions.

Table 2 shows the measured and predicted rotor pitch control settings. The "T75" variable is the rotor collective pitch at 0.75R. The "T1C" and "T1S" are the cosine and sine components of the rotor cyclic pitch inputs. Comparing the predicted model and full-scale pitch settings reveals that the model and full-scale rotors are trimmed to similar states with only small differences noted in the phasing of the cyclic pitches. Comparing predicted and measured settings

shows that the collective pitch is over-predicted by about 0.2°. The trend in collective pitch changes between the BL, MN, and MV cases is captured. The predicted amplitude of the cyclic pitch is seen to be within about 0.6° of the measured amplitude for each of the cases, though there are some differences between the model and full-scale phasing of the T1C and T1S components. Small differences in trim settings lead to differences in loading distributions on the rotor blades. These differences, in turn, result in wake strength, and therefore wake geometry differences. The radial loading differences lead to differences in trimmed rotor hub moments. In the model scale prediction, the hub moments are very small relative to the thrust when the final trim state was reached. In the full-scale prediction, the final hub moments were significantly larger in relation to the full-scale thrust, even though the trim tolerance requirement was met. With these trim differences in mind for the model and full-scale predictions, the aerodynamic loading and acoustics are examined for the full-scale rotor and compared to the predicted model scale rotor data.

Aerodynamics:

Figure 11 shows the full-scale predicted $C_N M^2$ compared to the predicted model scale data at 0.87R. The primary differences occur in the first rotor quadrant. There, loading pulses due to BVI are seen to be of similar character; however, the full-scale loading pulses have slightly different amplitudes and are shifted in azimuth location with respect to the model scale prediction. Since it is known that the BVI loading pulses are wake induced, and since these rotors are scaled versions of each other and trimmed to the similar conditions, it can be seen that the wake geometry and strength on the advancing side of the rotor are very sensitive to subtle changes in trim. Conversely, the retreating side loading is essentially identical between the rotors. This same trend will be seen in the next two figures as well.

Figure 12 compares the predicted model and full-scale loading for the MN case. As with the BL case, there are some differences on the advancing side. But, the differences are not as drastic as those seen in the BL case. The retreating side loading is nearly identical between the two rotors, as was the situation for the BL case. Figure 13 compares the predicted loading for the MV case. Similar to the BL case, the advancing side loading is seen to be sensitive to small trim differences, but the retreating side loading is nearly identical between the rotors. The next section will show the acoustic effects of these loading differences.

Mid-SPL:

Figure 14 compares the predicted model scale mid-SPL to the predicted full-scale mid-SPL. The overall directivity pattern from the model and full-scale predictions are very similar. Under the advancing side of the rotor, the full-scale predicted noise level is about 2 dB lower than the model scale predicted level. There is also a slight shift in the location of the maximum mid-SPL under the advancing side of the rotor. This is consistent with the differences in the loading seen above because the advancing side noise levels are dominated by loading on the advancing side of the rotor.

Figure 15 shows the mid-SPL for the MN case. This figure shows only a 1-2 dB lower noise level on the advancing side, with essentially no shift in the directivity pattern. Since the full-scale MN loading has slightly lower BVI loading levels on the advancing side than the predicted model scale, and since there is almost no shift in the BVI loading between the rotors, Figure 15 is consistent with the loading in Figure 12.

Figure 16 shows the mid-SPL for the MV case. As with Figure 15, there is little shift in the directivity pattern between the rotors, and there is only a 1-2 dB lower noise level on the advancing side under the rotor. These features again appear consistent with the loading information.

To further explore the acoustic differences, it is important to make sure that changes in decibel levels are associated with the same physical phenomena (Ref. 12). To accomplish this, the next section compares the full-scale and model scale predicted acoustic pressure time histories.

Acoustic pressure time histories:

To demonstrate that the same physical noise phenomena are being exhibited, acoustic pressure time histories are shown here. Figure 17 compares the full-scale and model scale acoustic pressure time history predictions for the BL case under the advancing side of the rotor. (This location is marked with a solid square symbol on Figure 14.) It is shown that the same primary BVI phenomena are being captured, though there are some differences in the low frequency acoustic character. Figure 18 and Figure 19 both show the same trends for the MN and MV cases, respectively.

The primary conclusion that can be drawn from the above sections is that, for an isolated rotor, the prediction scheme is scalable between a model scale rotor and a full-scale rotor. This demonstrates that, for the conditions examined, the full-scale isolated rotor prediction can be used to estimate flight effects. With prediction method fidelity demonstrated, the next section will examine variations in flight conditions.

Results: Full-scale flight variations

With the full-scale rotor prediction fidelity established above, the next logical step is to show that flight data trends with descent angle variations can be predicted. Spiegel, *et al* (Ref. 9) presents measured acoustic footprint trends with respect to rotor descent angle for a flight test of the BO-105 (full-scale rotor) vehicle. However, since the exact flight trim state and atmospheric conditions are not known at this time, the predicted trim state cannot be matched to measured data. In addition, the flight vehicle has a tail rotor, which is not being modeled in this study. With these differences in mind, the trends between the measured acoustic data and predicted acoustic data can be compared. To establish the trend with respect to rotor descent angle, the acoustic footprint variation is computed starting from the BL (6° descent) prediction used above. Two additional descent angles of 4° and 8°, respectively, are used as well.

For the comparisons between measurement and prediction, the same predicted comprehensive analysis data is used from the full-scale BL case above. Since there is a much larger distance from the rotor to the observers in this flight case, atmospheric propagation are included in the following results. Rotor tone noise predictions using WOPMOD are made for observers located on a hemispherical surface centered on the rotor hub. Here, a hemispherical radius of 10 rotor radii ($10R_{FS}$) is used. This hemispherical radius is twice the "arbitrarily chosen" (Ref. 30) value used in Reference 30, but the larger value is more consistent with recent (unpublished) studies. The computed data on the noise hemisphere is then used in RNM to compute the acoustic footprint on the ground.

Figure 20 shows the measured A-weighted, overall sound pressure level (L_A [dB]) noise contour data for the BL condition from the RONAP flight test (Ref. 9). (Note that for the remainder of this paper, the notation OASPL [dBA] will be used to represent the term L_A [dB].) This condition was chosen to closely match the BL condition shown in the "Results: Full-scale" section above. The vehicle is located at the origin and at an altitude of 120 meters. The horizontal axis represents the lateral distance from the vehicle in meters; positive numbers on this axis are on the starboard (or advancing side) of the rotor. The vertical axis represents the stream-wise distance from the vehicle in meters; positive numbers on this axis are forward of the vehicle. (Note: Pierre Spiegel provided Figure 20, Figure 22, and Figure 24 from Ref. 9 for this paper. The vertical axes in these three plots have been reversed from the direction in Reference 9 so that they match directions with all of the contour plots shown above).

Figure 21 shows the predicted OASPL [dBA] noise contours for the BL case. As expected, the highest predicted noise level is forward of, and to the advancing side of, the vehicle. It is seen that noise levels in the prediction are higher than in the measured data. However, since the exact trim state is not known, only the trends with descent angle can be compared. These variations are examined next.

Figure 22 shows the measured acoustic footprint from a nominally 3° descent angle condition. The noise level from this flight condition is lower than the BL condition and the directivity pattern has shifted toward the origin. Figure 23 shows the predicted OASPL [dBA] footprint for a 4° descent angle condition. The measured trend of having lower levels and shifting the directivity pattern toward the origin is well matched by the prediction.

Figure 24 shows the measured noise level and directivity patterns for a nominally 9° descent flight condition. Here, the noise levels increased on the advancing side of, and forward of, the rotor. Figure 25 shows the predicted quantities for an 8° descent. Again, the measured trends in noise level changes and in directivity pattern changes are well matched by the predictions.

Effect of HHC in flight:

With the fidelity of the full-scale rotor prediction shown above, an initial assessment of the effectiveness of the wind tunnel HHC conditions for a full-scale rotor can be computed. To accomplish this, noise predictions using the full-scale rotor model are made for the same scenario as used in Figure 21, except that HHC is applied as it was done in the wind tunnel. The noise contour results for the MN condition are shown in Figure 26 and those for the MV conditions are shown in Figure 27. For the MN condition (Figure 26), the noise radiated forward of, and to the advancing side of, the rotor is reduced by approximately 6 dBA relative to the BL condition in Figure 21. This is consistent with the measured trends shown in the HART-II data. The noise level radiated aft is relatively unchanged. From examination of the model rotor data it is known that the use of this MN value of HHC increases the blade-vortex miss-distance and moves the main BVI event more inboard on the blade compared to the BL condition (Ref. 18). Comparing the MV condition (Figure 27) to the BL condition, the noise radiated aft is also relatively unchanged. The noise radiated forward is slightly increased. Based on Ref. 18, this is because the BVI events tend to be slightly more intense, slightly more parallel, and slightly closer to the blade tip (where the Mach number is larger) compared to the BL condition. Even though the forward-radiated noise level increase is only slight in the MV case relative to the BL case, the ground area covered by the high-

noise level is substantially larger than that of the BL case.

Conclusions and Recommendations

Measured wind tunnel data for a model scale isolated rotor was used to demonstrate the NASA Aeroacoustic Prediction System. For the BL, MN, and MV cases, model scale predictions were shown to capture many major features of the measured airloads, acoustic footprints, and acoustic pressure time histories for the descent conditions examined. Full-scale isolated rotor predictions were performed for the same three conditions with dynamic scaling of the model rotor input data. Full-scale rotor predictions were also shown to capture the same measured features as the model scale predictions for these descent conditions. Particularly, the variation in predicted acoustic footprint with respect to rotor descent angle was shown to capture the same trend as seen in measured flight data.

This linkage provides confidence in a method to demonstrate the flight-effectiveness of tone noise reduction technologies that have previously been relegated to wind tunnel tests. Using this technique, it was shown that, under these descent conditions, acoustic footprint variations with respect to HHC on a full-scale (flight-scale) rotor are consistent with model scale wind tunnel measurements.

Though this method provides an important step towards a validated, full-scale, free-flight prediction scheme, much work remains to be done. In particular, the same type of isolated rotor link (made in this paper) needs to be shown for other flight conditions and as well as other rotorcraft noise sources to more fully address scaling issues as well as more fully validate prediction methods. This will be facilitated only by availability of accurate wind tunnel and flight data throughout the full flight regime.

Acknowledgements

The authors would like to thank Joon Lim and Wayne Johnson of NASA Ames Research Center for providing data for, and assistance with, the model-scale baseline CAMRAD-II input decks. Also, the authors would like to acknowledge Juliet Page of Wyle Labs for helpful discussions about RNM. Special thanks goes to Pierre Spiegel of the Institute of Aerodynamics and Flow Technology, DLR, Braunschweig, Germany for providing Figures 20, 22, and 24 from the RONAP flight data.

Primary funding for this work was provided under the NASA Runway Independent Aircraft (RIA) element of the Vehicle Systems Program.

References

1. Marcolini, M.A., Burley, C.L., Conner, D.A., Acree, Jr., C.W.: “Overview of Noise Reduction Technology of the NASA Short Haul (Civil Tiltrotor) Program,” SAE Paper 962273, International Powered Lift Conference, Jupiter, FL, November 8-10, 1996.
2. Hubbard, H.H. (editor): “Aeroacoustics of Flight Vehicles: Theory and Practice: Volume 1: Noise Sources,” NASA RP 1258, Vol. 1, pp 65-149, August 1991.
3. Splettstoesser, W.R., Kube, R., Seelhorst, U., Wagner, W., Boutier, A., Micheli, F., Mercker, E., Pengel, K.: “Higher Harmonic Control Aeroacoustic Rotor Test (HART) – Test Documentation and Representative Results,” IB 129-95/28, Deutche Forschungsanstalt für Luft- und Raumfahrt, December 1995.
4. Marcolini, M.A., Conner, D.A., Brieger, J.T., Becker, L.E., Smith, C.D.: “Noise Characteristics of a Model Tiltrotor,” 51st American Helicopter Society Forum, Fort Worth, TX, May 1995.
5. Kottapalli, S., Swanson, S., LeMasurier, P., Wang., J.: “Full Scale Higher Harmonic Control Research to Reduce Hub Loads and Noise,” 49th American Helicopter Society Forum, St. Louis, MO, May 1993.
6. Conner, D.A., Marcolini, M.A., Edwards, B.D., Brieger, J.T.: “XV-15 Tiltrotor Low Noise Terminal Area Operations,” 53rd American Helicopter Society Forum, Virginia Beach, VA, April 29 – May 1, 1997.
7. Conner, D.A., Marcolini, M.A., Decker, W.A., Cline, J.H., Edwards, B.D., Nicks, C.O., Klein, P.D.: “XV-15 Tiltrotor Low Noise Approach Operations,” 55th American Helicopter Society Forum, Montreal, Quebec, Canada, May 25-27, 1999.
8. Conner, D.A., Edwards, B.D., Decker, W.A., Marcolini, M.A., Klein, P.D.: “NASA/Army/Bell XV-15 Tiltrotor Low Noise Terminal Area Operations Flight Research Program,” Journal of the American Helicopter Society, 47(4), pp. 219-232, October 2002.
9. Spiegel, P., Buchholz, H., Splettstoesser, W.: “The ‘RONAP’ Aeroacoustic Flight Tests with a Highly Instrumented BO 105 Helicopter,” 59th American Helicopter Society Forum, Phoenix, AZ, May 6-8, 2003.
10. Schmitz, F.H., Yu, Y.H.: “Helicopter Impulsive Noise: Theoretical and Experimental Status,” NASA TM 84390, November 1983.
11. Brooks, T.F., Boyd, Jr., D.D., Burley, C.L., Jolly, Jr., J.R.: “Aeroacoustic Codes for Rotor Harmonic and BVI Noise – CAMRAD.Mod1/HIRES,” AIAA/CEAS 2nd

Aeroacoustics Conference, State College, PA, May 1996.
12. Boyd, Jr., D.D., Burley, C.L.: "Analysis of Measured and Predicted Acoustics from an XV-15 Flight Test," 57th American Helicopter Society Forum, Washington, D.C., May 9-11, 2001.
13. Lim, J.W., Tung. C., Yu, Y.H., Burley, C.L., Brooks, T.F., Boyd, Jr., D.D., van der Wall, B., Schneider, O., Richard, H., Raffel, M., Beaumier, P., Bailly, J., Delrieux, Y., Pengal, K., Mercker, E.: "HART-II – Prediction of Blade Vortex Interaction Loading," 29th European Rotorcraft Forum, Friedrichshafen, Germany, September 16-18, 2003.
14. Burley, C.L., Marcolini, M.A., Brooks, T.F., "Tiltrotor Aeroacoustic Code (TRAC) Predictions and Comparison with Measurements," Journal of the American Helicopter Society, pp. 80-90, April 2000.
15. JanakiRam, R.D., Khan, H.: "Prediction and Validation of Helicopter Descent Flyover Noise," 56th American Helicopter Society Forum, Virginia Beach, VA, May 2-4, 2000.
16. Boyd, Jr., D.D.: "Challenges in Rotorcraft Acoustic Flight Prediction and Validation," AIAA Paper 2003-0709, 41st AIAA Aerospace Sciences Meeting, Reno, NV, January 6-9, 2003.
17. Yu, Y.H., Tung, C., van der Wall, B., Pausder, H., Burley, C.L., Brooks, T.F., Beaumier, P., Delrieux, Y., Mercker, E., Pengal, K.: "The HART-II Test: Rotor Wakes and Aeroacoustics with Higher-Harmonic Pitch Control (HHC) Inputs – The Joint German/French/Dutch/U.S. Project," 58th American Helicopter Society Forum, Montreal, Canada, May 2002.
18. van der Wall, B.G., Junker, B., Burley, C.L., Brooks, T.F., Yu, Y., Tung, C., Raffel, M., Hugues, R., Wagner, W., Mercker, E., Pengel., K., Holthusen, H., Beaumier, P., Delrieux, Y.: "The HART II Test in the LLF of the DNW – A Major Step Towards Rotor Wake Understanding," 28th European Rotorcraft Forum, Bristol, UK, September, 17-20, 2002.
19. Johnson, W.J.: "CAMRAD-II: Comprehensive Analytical Model of Rotorcraft Aerodynamics and Dynamics, Release 4.2 (Volumes I-IX)," Johnson Aeronautics, 2003.
20. Johnson, W.J.: "Influence of Wake Models on Calculated Tiltrotor Aerodynamics," American Helicopter Society Aerodynamics, Acoustics, and Test and Evaluation Specialists' Meeting, San Francisco, CA, January 23-25, 2002.
21. Brentner, K.S.: "Prediction of Helicopter Rotor Discrete Frequency Noise," NASA TM 87721, October 1986.
22. Page, J.A., Plotkin, K.J., Downing, J.M.: "Rotorcraft Noise Model User's Guide," Wyle Research Report WR 00-20, August 2000.
23. Conner, D.A., Page, J.A.: "A Tool for Low Noise Procedures Design and Community Noise Impact Assessment: The Rotorcraft Noise Model (RNM)," AIAA Paper T213-6, Heli Japan 2002, Tochigi, Japan, November 11-13, 2002.
24. Zorumski, W.E.: "Aircraft Noise Prediction Program Theoretical Manual," NASA TM 83199 (Part 1), 1982.
25. Acoustical Society of America National Standard, "Method for the Calculation of the Absorption of Sound by the Atmosphere," ANSI S1.26-1978.
26. Chien, C.F., Soroka, W.W.: "Sound Propagation Along An Impedance Plane,"
27. Chessel, C.I.: "Propagation of Noise Along a Finite Impedance Boundary," Journal of the Acoustical Society of America, 62(4), pp. 825-834, October 1977.
28. Daigle, G.A., Embleton, T.F.W., and Piercy, J.E.: "Some Comments on the Literature of Propagation Near Boundaries of Finite Acoustical Impedance," Journal of the Acoustical Society of America, 66(3), pp. 918-919, September 1979.
29. Rasmussen, K.B.: "The Effect of Terrain Profile on Sound Propagation Outdoors", Danish Acoustical Institute Technical Report 111, January 1984.
30. Wilson, M.R., Mueller, A.W., Rutledge, C.K.: "A New Technique for Estimating Ground Footprint Acoustics for Rotorcraft Using Measured Sound Fields," American Helicopter Society Vertical Lift Aircraft Design Conference, San Francisco, CA, January 18-20, 1995.

Figures

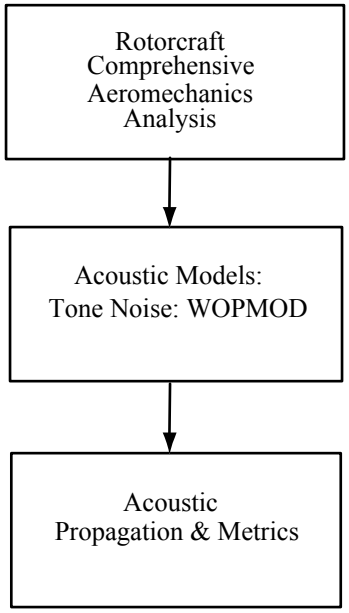

Figure 1: Outline of NASA Aeroacoustic Prediction System.

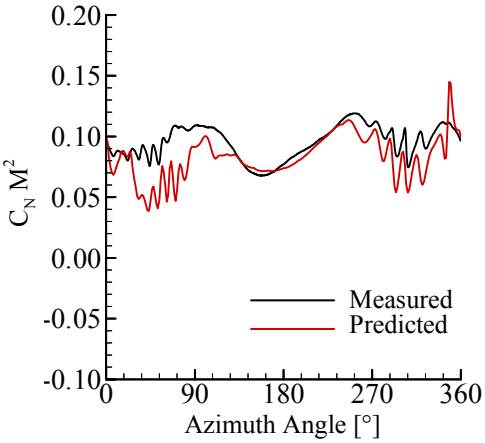

Figure 2: Model scale – measured and predicted normal force coefficient times Mach number squared at 0.87R for BL condition.

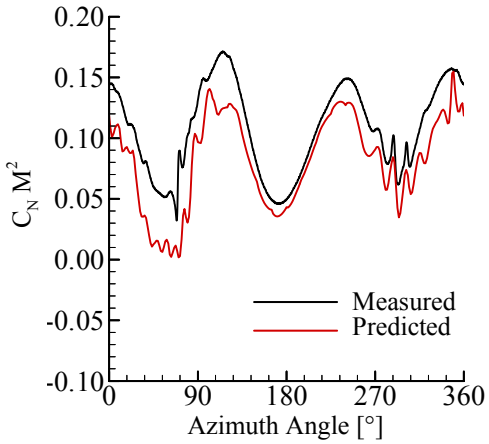

Figure 3: Model scale – measured and predicted normal force coefficient times Mach number squared at 0.87R for MN condition.

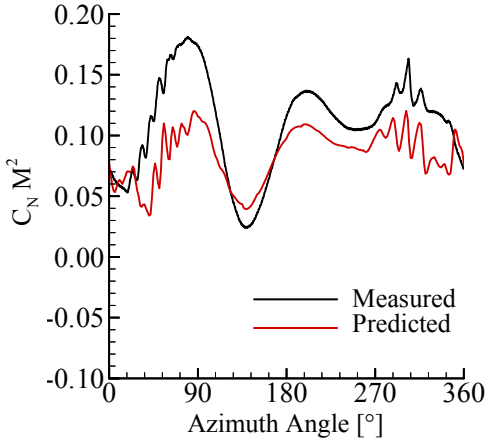

Figure 4: Model scale – measured and predicted normal force coefficient times Mach number squared at 0.87R for MV condition.

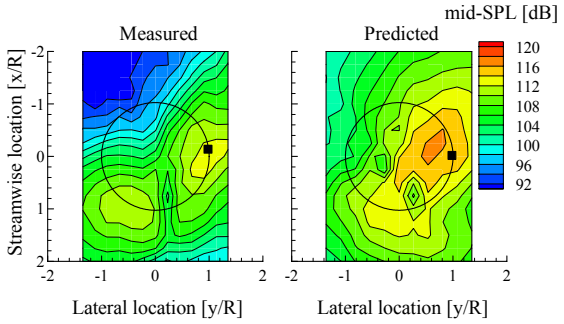

Figure 5: Model scale – measured and predicted mid-SPL [dB] footprint for the BL condition.

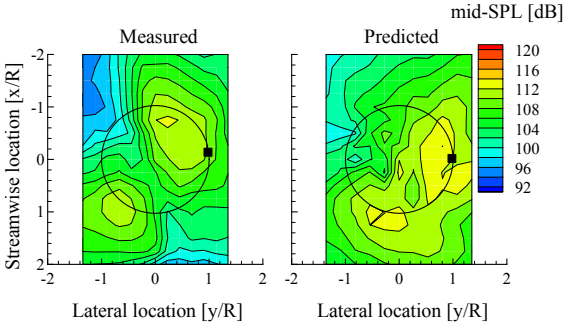

Figure 6: Model scale – measured and predicted mid-SPL [dB] footprint for the MN HHC condition.

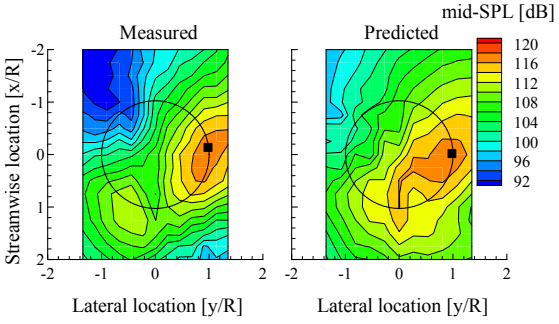

Figure 7: Model scale – measured and predicted mid-SPL [dB] footprint for the MV HHC condition.

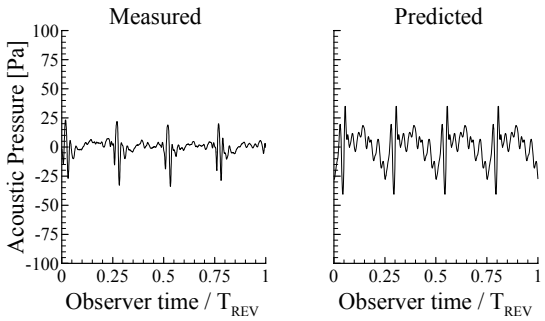

Figure 8: Model scale – measured and predicted acoustic pressure time histories for the BL case. The location is marked by the black square in Figure 5.

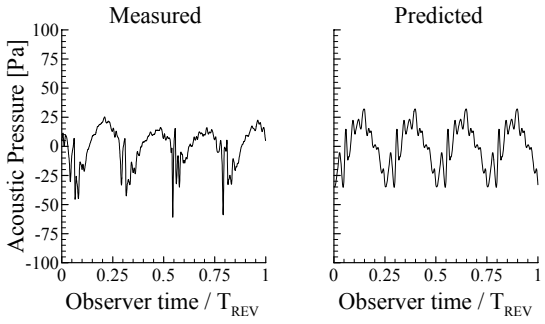

Figure 9: Model scale – measured and predicted acoustic pressure time histories for the MN condition; same location as above.

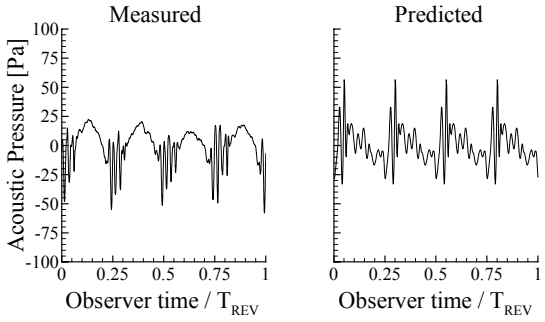

Figure 10: Model scale – measured and predicted acoustic pressure time histories for the MV condition; same location as above.

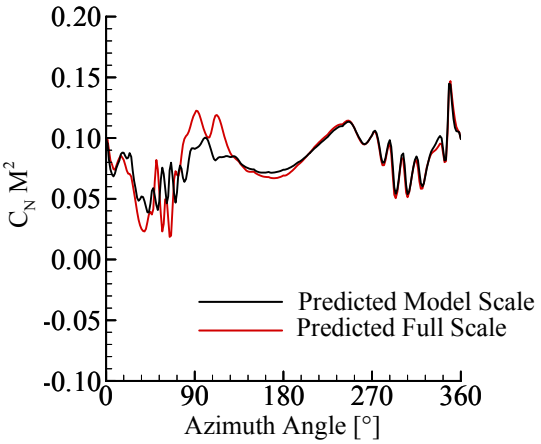

Figure 11: Comparison of predicted model scale and predicted full-scale normal force coefficient times Mach number squared at 0.87R for BL condition.

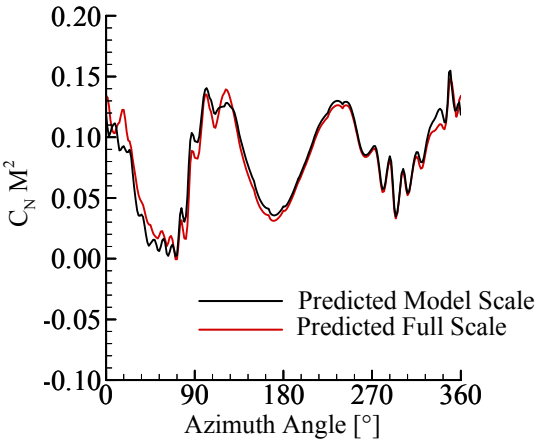

Figure 12: Comparison of predicted model scale and predicted full-scale normal force coefficient times Mach number squared at 0.87R for MN condition.

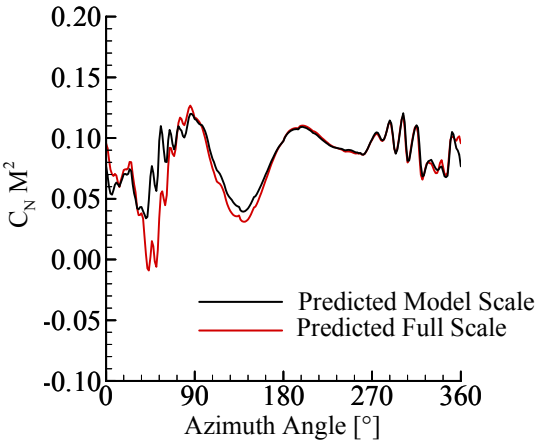

Figure 13: Comparison of predicted model scale and predicted full-scale normal force coefficient times Mach number squared at 0.87R for MV condition.

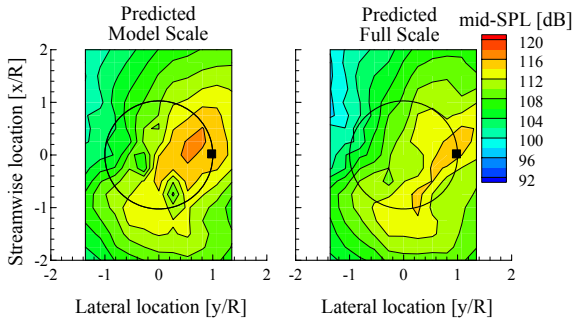

Figure 14: Comparison of predicted model scale and predicted full-scale mid-SPL [dB] footprint for the BL condition.

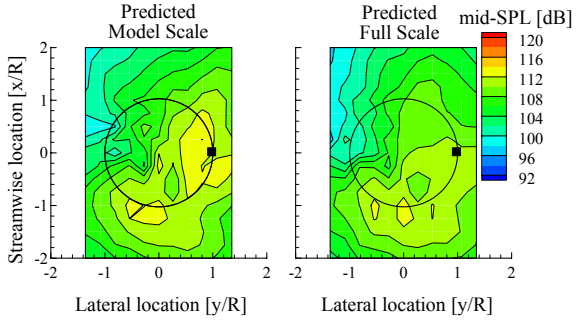

Figure 15: Comparison of predicted model scale and predicted full-scale mid-SPL [dB] footprint for the MN HHC condition.

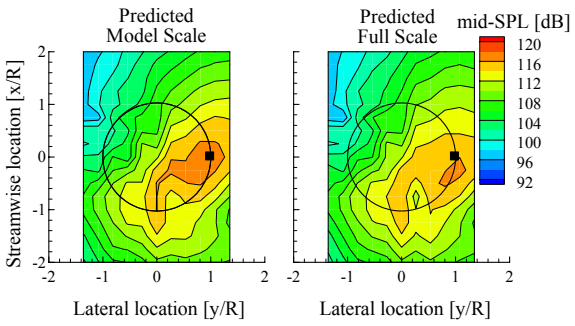

Figure 16: Comparison of predicted model scale and predicted full-scale mid-SPL [dB] footprint for the MV HHC condition.

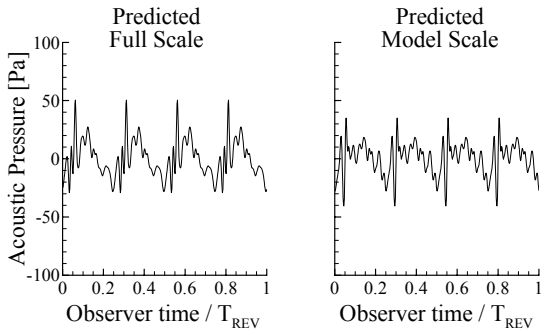

Figure 17: Comparison of predicted full-scale and predicted model scale acoustic pressure time histories for the BL case.

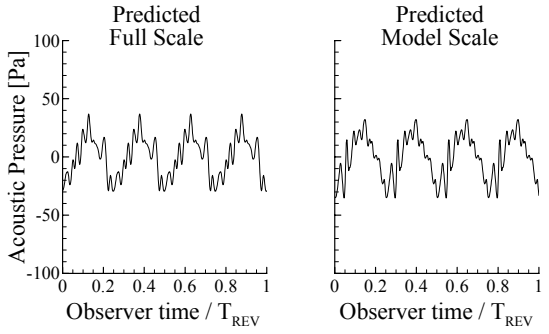

Figure 18: Comparison of predicted full-scale and predicted model scale acoustic pressure time histories for the MN case.

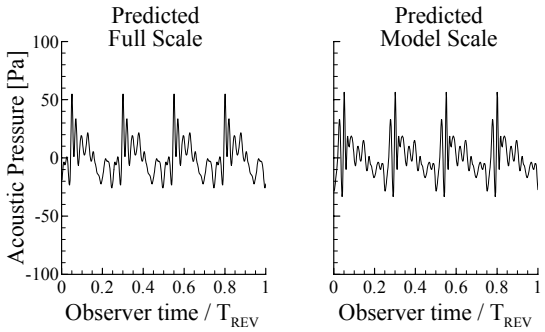

Figure 19: Comparison of predicted full-scale and predicted model scale acoustic pressure time histories for the MV case.

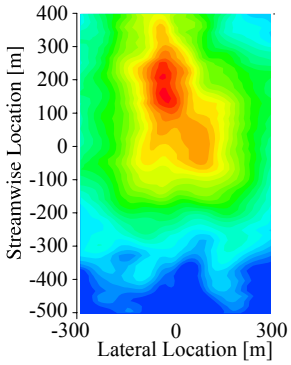

Figure 20: Full-scale flight vehicle measured OASPL [dBA] acoustic footprint for nominal 6° descent, BL case (figure provided by Pierre Spiegel (Ref. 9).

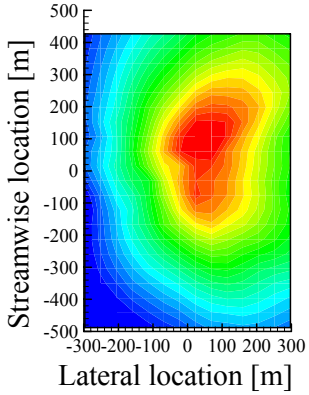

Figure 21: Predicted OASPL [dBA] acoustic footprint for nominal 6° descent full-vehicle condition.

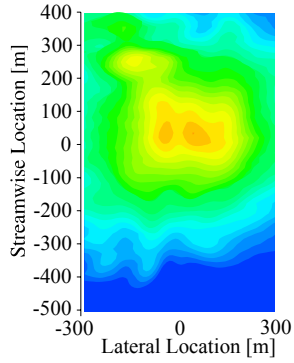

Figure 22: Full-scale flight vehicle measured OASPL [dBA] acoustic footprint for nominal 3° descent condition (figure provided by Pierre Spiegel (Ref. 9).

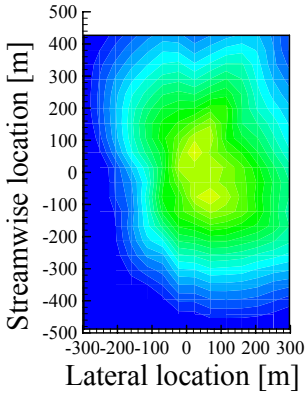

Figure 23: Predicted OASPL [dBA] acoustic footprint for a 4° descent condition.

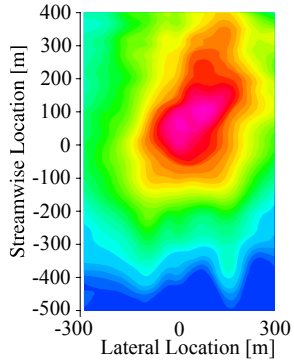

Figure 24: Full-scale flight vehicle measured OASPL [dBA] acoustic footprint for nominal 9° descent condition (figure provided by Pierre Spiegel (Ref. 9).

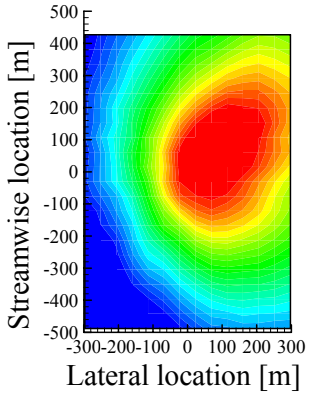

Figure 25: Predicted OASPL [dBA] acoustic footprint for an 8° descent condition.

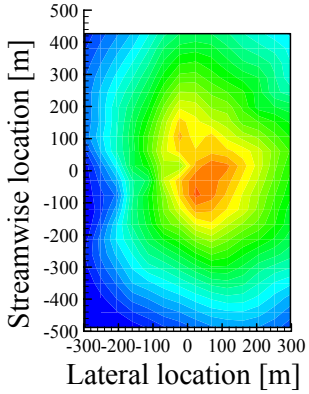

Figure 26: Predicted OASPL [dBA] acoustic footprint for the MN HHC flight condition.

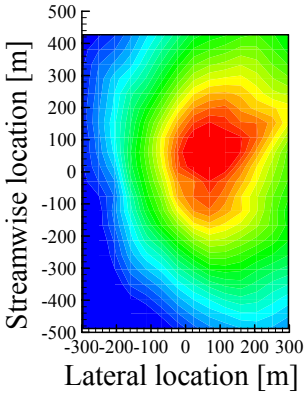

Figure 27: Predicted OASPL [dBA] acoustic footprint for the MV HHC flight condition.